PARTICLE-LEVEL SIMULATIONS OF FLOCCULATION IN A FIBER SUSPENSION FLOWING THROUGH A DIFFUSER

by

Jelena S. ANDRIĆ[a*], Stefan B. LINDSTRÖM[b], Srdjan M. SASIC[a], Håkan NILSSON[a]

[a] Department of Applied Mechanics, Chalmers University of Technology, 412 96 Göteborg, Sweden
[b] Department of Management and Engineering, The Institute of Technology, Linköping University, 581 83 Linköping, Sweden

Invited original scientific paper
DOI:

We investigate flocculation in dilute suspensions of rigid, straight fibers in a decelerating flow field of a diffuser. We carry out numerical studies using a particle-level simulation technique that takes into account the fiber inertia and the non-creeping fiber–flow interactions. The fluid flow is governed by the Reynolds-averaged Navier–Stokes equations with the standard k-ω eddy-viscosity turbulence model. A one-way coupling between the fibers and the flow is considered with a stochastic model for the fiber dispersion due to turbulence. The fibers interact through short-range attractive forces that cause them to aggregate into flocs when fiber–fiber collisions occur. We show that ballistic deflection of fibers greatly increases the flocculation in the diffuser. The inlet fiber kinematics and the fiber inertia are the main parameters that affect fiber flocculation in the pre-diffuser region.

Key words: *fiber suspension, ballistic deflection, decelerating flow, flocculation, diffuser.*

Introduction

Fiber suspension flows are encountered in various industrial processes such as dry-forming of pulp mats, molding of fiber-reinforced composites, pulp production and papermaking, and water treatment processing. In these applications fiber flocculation significantly affects the performance of the involved processes and the product quality. Preventing flocculation is essential in dry-forming of pulp mats since a uniform spatial distribution of the fibers usually improves the final product quality [1]. On the other hand, flocculation is desirable in water purification and wastewater treatment, where particles aggregate into flocs that are then removed by sedimentation or filtration [2, 3]. There is therefore a need to predict and control flocculation in flowing suspensions. This requires a detailed understanding of complex fiber–fiber and fiber–flow interactions.

The effects of various fiber parameters and inter-fiber forces on fiber flocculation have been analyzed in literature. Schmid *et al.* [4] showed that frictional forces lead to floc formation, while Switzer and Klingenberg [5] demonstrated the importance of fiber shape and deformability on their flocculation.

* Corresponding author: jelena.andric@chalmers.se

Fiber orientation distribution and floc formation have also been studied in turbulent flow fields. Do-Quang *et al.* [6] employed direct numerical simulations to account for contact and lubrication forces between rigid fibers suspended in a turbulent channel flow. The study showed that the fibers tend to accumulate in high-speed streaks in the near-wall regions. Jafari *et al.* [7] modeled the formation and breakup of fiber flocs caused by the hydrodynamic forces in a turbulent channel flow. Fiber flocculation has also been modeled using the population balance method [8, 9] showing that the floc size distribution is greatly affected by the local flow properties.

It was recently demonstrated that the fiber trajectories of inert fibers transported in a decelerating flow field, as found in a diffuser, may significantly deviate from the streamlines of the flow [10]. This phenomenon was referred to as *ballistic deflection*, and it was shown to be generated by the velocity difference between the fiber and the carrying fluid and the anisotropic hydrodynamic resistance of the fiber. In the present work we investigate the effects of ballistic deflection on flocculation of rigid, straight fibers in an incompressible decelerating flow. The numerical study is carried out using a particle-level simulation technique. Both the fiber and the flow inertia are taken into account. We consider dilute fiber suspensions and thus a one-way coupling between the fibers and the flow is assumed. Numerical simulations consider different kinematic conditions when the fibers are reinjected at the diffuser inlet. We analyze the significance of these kinematic disturbances as well as the influence of fiber inertia on the flocculation process.

Fiber suspension model

The flowing fiber suspension is modeled using a Lagrangian fiber model together with a solution of the Reynolds-averaged Navier–Stokes (RANS) equations for the carrying fluid. The model includes one-way fluid–fiber interactions and a contact model for fiber–fiber interactions. We here present a brief description of the fluid model and the fiber model, followed by a description of the fiber–flow and fiber–fiber interactions.

Fluid model

The fluid flow is governed by the steady-state, incompressible, two-dimensional RANS equations. The mass and momentum conservation equations read

$$\nabla \cdot \vec{U} = 0, \tag{1}$$

$$\vec{U} \cdot \nabla \vec{U} = \nu_{\text{eff}} \nabla^2 \vec{U} - \nabla p. \tag{2}$$

Here $\vec{U}$ is the fluid velocity, p is the kinematic pressure, t is the time, and ν_{eff} is the effective kinematic viscosity that includes contributions from both laminar viscosity and turbulence. Turbulence is taken into account using the standard k-ω turbulence model [11]. This model includes two additional transport equations for the turbulence kinetic energy k and specific dissipation ω. The fibers are affected by the modeled turbulence by adding a fluctuating component to the interpolated RANS velocity, as described earlier in the paper, *i.e.*

$$\vec{u} = \vec{U} + \tilde{\vec{u}}. \tag{3}$$

Fiber model

We model rigid fibers as described by Lindström and Uesaka [12] and Andrić *et al.* [13]. Each fiber is modeled as a chain of N rigid, and rigidly connected, fiber segments, see fig. 1. This discretization is made to take into account the flow variations along the fiber length. The center of mass of segment i

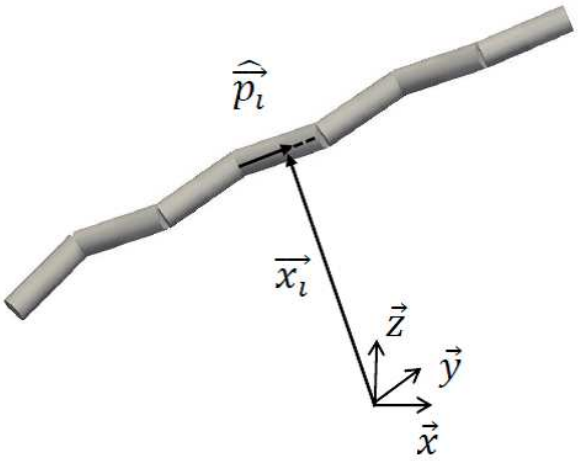

Figure 1. Fiber geometry illustration for a general case of a non-straight fiber making the segments visible. The present work only deals with straight fibers.

is denoted by $\vec{x}_i$ and the orientation vector is denoted by $\hat{\vec{p}}_i$. This work is concerned with straight fibers where all segments have the same orientation $\hat{\vec{p}}$, diameter d, length l, and density ρ_f.

The linear and angular momentum equations are formulated for each fiber, *i.e.*

$$m\ddot{\vec{x}}_G = \sum_{i=1}^{N} \vec{F}_i^h, \tag{4}$$

$$\frac{\partial}{\partial t}(\boldsymbol{I}_G \cdot \vec{\omega}) = \boldsymbol{I}_G \cdot \dot{\vec{\omega}} + \vec{\omega} \times (\boldsymbol{I}_G \cdot \vec{\omega}) = \sum_{i=1}^{N} \left(\boldsymbol{T}_i^h + (\vec{x}_i - \vec{x}_G) \times \vec{F}_i^h \right). \tag{5}$$

Here $\vec{x}_G$ is the center of mass of the fiber, m is its mass, and $\vec{\omega}$ is its angular velocity. $\boldsymbol{I}_G$ is the inertia tensor of the fiber with respect to its center of mass and a global inertial frame of reference. $\vec{F}_i^h$ and $\vec{T}_i^h$ are the total hydrodynamic drag force and torque, respectively, exerted by the fluid on segment i.

Fiber–flow and fiber–fiber interactions

Since the flow of the carrying fluid is computed using a RANS simulation, the turbulent eddies are not resolved. Consequently, to capture the effects of the flow fluctuations on the fiber motion, it is necessary to construct a representation of the fluctuating flow field that is superimposed onto the mean flow field. We employ the stochastic model for the flow fluctuations proposed by Gosman and Ioannides [14]. This model adds a fluctuation component to the mean flow velocity at the segment center of mass, *i.e.*

$$\vec{u}(\vec{x}_i) = \vec{U}(\vec{x}_i) + \tilde{\vec{u}}^{fiber}. \tag{6}$$

The velocity fluctuation is estimated for each fiber as

$$\tilde{\vec{u}}^{fiber} = \vec{\Psi}\sqrt{\frac{2}{3}\frac{\sum_{i=1}^{N} k(\vec{x}_i)}{N}}, \tag{7}$$

where the components of the vector $\vec{\Psi} = (\Psi_1, \Psi_2, \Psi_3)$ are random numbers from a Gaussian distribution of mean zero and variance one, and where $k(\vec{x}_i)$ is the modeled turbulence kinetic energy at segment i. We thus assume that we have the same flow fluctuations along the fiber length. The fluctuating flow velocity at a floc, $\tilde{\vec{u}}^{floc}$ is computed similarly as for a single fiber (eq. (6)), but summing over all segments of all the fibers in the floc, again assuming the same flow fluctuations across all the fibers in each floc. A new random vector $\vec{\Psi}$ is generated for each fiber/floc at each time step. It should be noted that the present stochastic model involves the translational dispersion of fibers, but neglects the changes in the fiber orientation due to the velocity fluctuations.

We define the fiber Reynolds number based on the relative velocity between the fiber and the flow as

$$\mathrm{Re_f} = \frac{d\left|\dot{\vec{x}}_G - \vec{U}(\vec{x}_G)\right|}{\nu}, \tag{8}$$

where $\vec{U}(\vec{x}_G)$ is the RANS fluid flow velocity interpolated at the fiber center of mass, and ν is the kinematic viscosity of the fluid. The hydrodynamic force and torque are approximated as a sum of the viscous ($\mathrm{Re_f} \ll 1$) and the dynamic drag ($\mathrm{Re_f} \gg 1$) contributions, as previously proposed by Lindström and Uesaka [12], *i.e.*

$$\vec{F}_i^h = \vec{F}_i^{h,\upsilon} + \vec{F}_i^{h,I}, \tag{9}$$

$$\vec{T}_i^h = \vec{T}_i^{h,\upsilon} + \vec{T}_i^{h,I}. \tag{10}$$

The viscous drag force $\vec{F}^{h,\upsilon}$ and torque $\vec{T}^{h,\upsilon}$ are approximated by those of an isolated prolate spheroid derived by Kim and Karilla [15], and further described by Lindström and Uesaka [12] and Andrić *et al.* [13]. The expressions for the dynamic force and torque in the limit of high relative velocity were previously derived [12] as

$$\vec{F}_i^{h,I} = \boldsymbol{A}_i^I \cdot [\vec{u}(\vec{x}_i) - \dot{\vec{x}}_i], \tag{11}$$

$$\vec{T}_i^{h,I} = \boldsymbol{C}_i^I \cdot [\vec{\Omega}(\vec{x}_i) - \vec{\omega}] + \boldsymbol{H}_i^I : \boldsymbol{G}(\vec{x}_i). \tag{12}$$

Here

$$\vec{\Omega}(\vec{x}_i) = \nabla \times \frac{\vec{U}(\vec{x}_i)}{2} \tag{13}$$

and

$$\boldsymbol{G}(\vec{x}_i) = \frac{1}{2}\left(\nabla\vec{U}(\vec{x}_i) + \nabla\vec{U}(\vec{x}_i)^{\mathrm{T}}\right) \tag{14}$$

are the flow vorticity and the strain rate tensor at the center of mass of segment i, respectively. Those two terms are based on the RANS velocity field $\vec{U}$ directly, since their evaluations require a smooth velocity

field. The approximations of the dynamic resistance tensors read

$$\boldsymbol{A}_i^I = \frac{1}{2} C_D^I \rho d l \upsilon_{\perp,i} \left(\boldsymbol{\delta} - \hat{\vec{p}}\hat{\vec{p}}^{\mathrm{T}} \right), \tag{15a}$$

$$\boldsymbol{C}_i^I = \frac{1}{24} C_D^I \rho d l^3 \upsilon_{\perp,i} \left(\boldsymbol{\delta} - \hat{\vec{p}}\hat{\vec{p}}^{\mathrm{T}} \right), \tag{15b}$$

$$\boldsymbol{H}_i^I = \frac{1}{24} C_D^I \rho d l^3 \upsilon_{\perp,i} \left[\left(\boldsymbol{\varepsilon} \cdot \hat{\vec{p}} \right) \hat{\vec{p}} \right]. \tag{15c}$$

Here $\upsilon_{\perp,i} = |(\boldsymbol{\delta} - \hat{\vec{p}}\hat{\vec{p}}^{\mathrm{T}}) \cdot [\vec{u}(\vec{x}_i) - \dot{\vec{x}}_i]|$ is the transverse velocity of the fluid relative to the fiber segment and $\boldsymbol{\varepsilon}$ is the permutation tensor. The derivation of the dynamic resistance tensors is based on the well-known proportionality of the drag force per unit length to the square of the fluid velocity component normal to the cylinder axis and the nearly constant drag coefficient $C_D^I \approx 1$ in the range $10^2 < \mathrm{Re_f} < 3 \cdot 10^5$ [16]. Further details of the derivation and validation of the total drag force and torque can be found in the work of Lindström and Uesaka [12].

Fiber contacts are detected using the shortest distance algorithm [4, 12, 17]. Each fiber is either isolated or part of a floc, within which all fiber segments have fixed positions and orientations relative to each other. When two segments from different fibers or flocs come into contact they instantly merge into one single floc by freezing the relative fiber segment positions of both fibers and flocs. Thus the floc is a rigid body system and its motion is also governed by eqs. (4) and (5) formulated for the center of mass of the floc.

The equations of motion of fibers/flocs are discretized in time. More details about the numerical schemes and the time step constraints can be found in the previous work of Andrić *et al.* [13]. The discretized equations are solved for the linear and angular velocities of fibers and flocs that are then used to compute new fiber/floc positions and orientations.

Fluid flow results and validation

The fiber motion is integrated in the turbulent flow of an asymmetric planar diffuser. This flow case geometry is chosen because it represents well the flow conditions in the actual dry-forming process. Figure 2 illustrates the computational domain based on the experimental setup of Buice and Eaton [18]. The inlet section is made long to ensure a fully developed flow at the diffuser inlet. A constant velocity profile that corresponds to the inlet bulk velocity $U_b = 28$ m/s was specified at the inlet boundary. The Reynolds number $\mathrm{Re} = U_b H/\nu = 18000$ matches the experimental value, where the inlet height $H = 0.01$ m and ν is the kinematic viscosity of the fluid. The inlet turbulence kinetic energy and specific dissipation are specified to $k = 0.0001$ m^2/s^2 and $\omega = 84000$ s^{-1}, respectively. The second-order linear-upwind scheme is used for the convection terms in the momentum and turbulence equations [19]. The SIMPLE algorithm is used for the pressure-velocity coupling [20]. The computational mesh consists of 420×80 cells and it is graded to resolve the near-wall gradients. The first cell centers are typically located at $y^+ \approx 1$.

The steady-state flow results are validated using the experimental results of Buice and Eaton [18] and Obi *et al.* [21]. A coordinate x is introduced in the longitudinal direction with $x = 0$ at the beginning of the expansion of the diffuser. Figure 3 shows a comparison between the computed and the experimental longitudinal velocity profiles at different positions along the diffuser. The longitudinal velocity profiles are very well-predicted, with a recirculation region contacting the lower boundary of the expan-

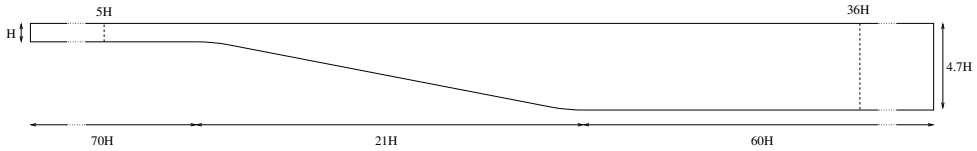

Figure 2. Asymmetric planar diffuser. The vertical dotted lines indicate the region where the fibers are present.

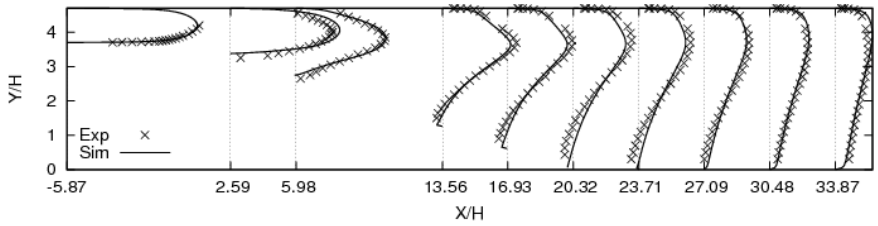

Figure 3. A comparison between the simulated (Sim) and experimental (Exp) results for the longitudinal velocity profiles at different locations along the diffuser.

sion. The turbulence kinetic energy profiles are presented in fig. 4. The turbulence kinetic energy is over-predicted at two cross-sections near the entrance of the diffuser, as also predicted by El-Behery and Hamed [22]. The discrepancy is due to the choice of turbulence model. Nonetheless, it is our judgment that the computed flow field is sufficiently accurate for the present study of fiber motion and fiber floc formation.

Fiber suspension simulation cases and definitions

The computational domain of fiber flocculation simulations is restricted to $[-5H, 36H]$ in the longitudinal diffuser direction, see fig. 2. The inlet plane $x = -5H$ is located at some distance upstream the diffuser inlet, and the outlet plane $x = 36H$ is located at some distance downstream the recirculation region. The fibers are initiated uniformly randomized, both in terms of position and orientation, in the upper region of the diffuser $[-5H, 36H] \times [0, H] \times [-2H, 2H]$. This initial fiber configuration is chosen to faster reach a steady-state distribution. We performed a test simulation where the fibers were initiated randomized in the entire domain, and observed that the fibers end up the same way, but slower. The fiber motion is made periodic in the spanwise direction z so that a fiber or a floc that crosses any of

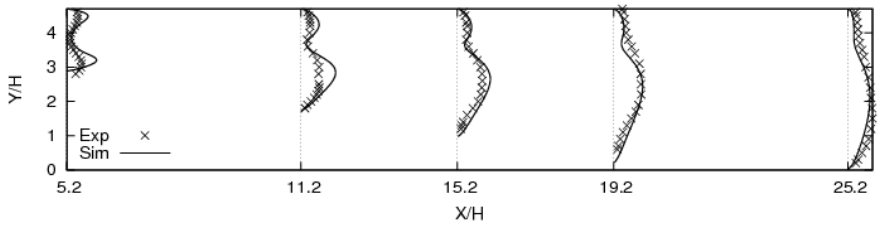

Figure 4. A comparisson between the simulated (Sim) and experimental (Exp) results for the turbulence kinetic energy profiles at different locations along the diffuser.

the planes $z = \pm 2H$ is moved to the corresponding opposite plane with all the other properties being preserved. Fibers that either cross the outlet plane $x = 36H$ or approach the walls reenter the diffuser as isolated fibers with a random uniform spatial distribution at the inlet plane, keeping the total number of fibers constant during the simulation. The effect of the reinjection approach is studied by three cases with linear velocity, angular velocity, and orientation according to:

1. Case 1: The linear velocity of each segment is set to $\vec{U}(\vec{x}_G)$; the angular fiber velocity is set to zero; the fiber orientation is set randomly.

2. Case 2: The longitudinal linear velocity component of each segment is set to that of $\vec{U}(\vec{x}_G)$ and the other two velocity components are set to zero; the angular fiber velocity is set to zero; the fiber orientation is set randomly.

3. Case 3: The linear velocity of each segment is set to $\vec{U}(\vec{x}_G)$; the angular fiber velocity $\vec{\omega}$ is initialized by $\vec{\Omega}(\vec{x}_G)$ when solving the discretized equations of motion, where Ω is the fluid vorticity (see eq. (13)) ; the fiber is oriented in the longitudinal direction of the diffuser.

The fiber properties are consistent with those of softwood fibers that are commonly used in the dry-forming process. Each fiber comprises five segments with diameter $d = 20$ μm, length $l = 0.2$ mm and density $\rho_{\mathrm{f}} = 1380$ kg/m^3. These fiber properties are used in all simulations unless stated otherwise.

Results and discussion

We analyze fiber flocculation for the simulation cases described above and investigate the influence of fiber inertia on the flocculation process.

Fiber flocculation

The fiber–fiber and fiber–floc contacts are detected at each time step and the contacting fibers are merged into larger flocs as described earlier in the paper. We identify different species of flocs F_j, where $j \in [1,n]$ is the number of fibers in a floc. The part of the computational domain where the fibers are present is divided into 128 equally thick control volumes along the flow direction. We compute the mass fraction of species F_j for each control volume as

$$\phi_j = \frac{jN_j}{\sum_{q=1}^{n} qN_q}, \tag{16}$$

where N_j is the time-averaged number of F_j floc species in a given control volume. The nominator is thus the time-averaged number of fibers that are in flocs of j fibers. The denominator gives the time-averaged total number of fibers in the control volume, in any kind of floc. The dimensionless flocculation rate of F_j is defined as

$$\phi_j'^{*} = \frac{d\phi_j}{dx}H. \tag{17}$$

We analyze the formation of floc species F_2 along the length of the diffuser. The development of the mass fraction ϕ_2 is shown in fig. 5. The flow field in the inlet channel region $-5 < x/H < 0$ is nearly uniform and aligned with the channel. However, we observe a rapid increase in the mass fraction ϕ_2 for Cases 1 and 2 in the inflow channel region $-5 < x/H < 0$, and the beginning of the diffuser section, $0 < x/H < 5$. The random fiber orientation increases the formation of flocs right after the reinjection. The dimensionless flocculation rate $\phi_2'^{*}$ decreases in the region $-5 < x/H < 5$, see fig 6. For Case

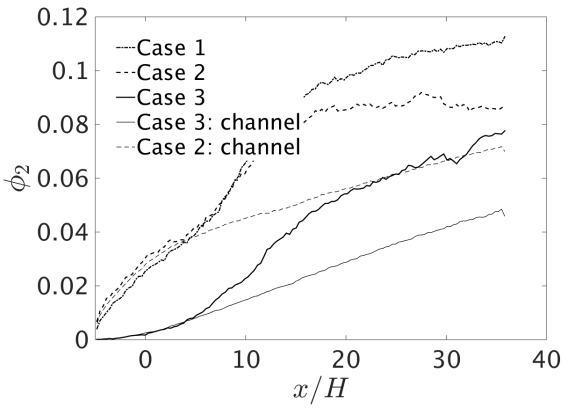

Figure 5. Mass fraction ϕ_2 of floc species F_2 along the length of the diffuser for different reinjection cases. The result for a channel flow is included for comparison.

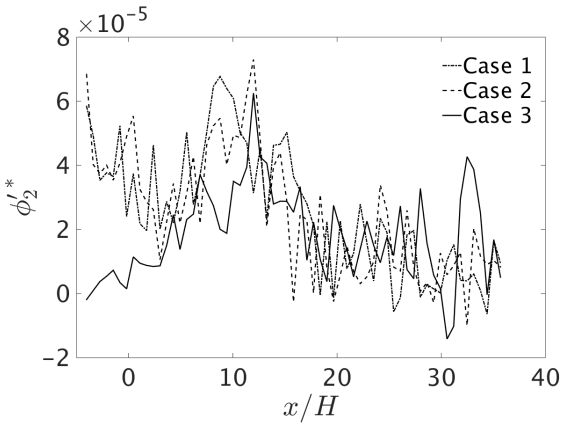

Figure 6. Flocculation rate $\phi_2'^*$ along the length of the diffuser for different fiber reinjection cases.

3, where the reinjected fibers are aligned with the flow direction, there is a slight increase in the mass fraction and the flocculation rate until $x/H < 5$. An elevation in the dimensionless flocculation rate $\phi_2'^*$ and the mass fraction ϕ_2 is then observed in the diffuser section downstream from $x/H = 5$ for all three cases. As the mean flow velocities decrease through the diffuser section, the velocity gradient in the flow direction and the inertia of the fibers contribute to a velocity difference between the fibers and the flow. This relative velocity together with the oriented hydrodynamic resistance tensor lead to ballistic deflection of fibers [10], which is believed to significantly increase the collisions between the fibers and thus contributes to the flocculation. It should be noted that the fiber flocculation rate downstream $x/H = 5$ is similar for all the cases, see fig. 6. This observation strongly suggests that ballistic deflection of fibers dominates the flocculation process independently of the inlet kinematics of the reinjected fibers. To further analyze the effect of the flow parameters on fiber flocculation, we carried out the same analysis as for Cases 2 and 3 but for a straight channel with height H. The results for Cases 2 and 3 for the straight channel are scaled by the fiber number density ratio between the diffuser and the channel, and are included in fig. 5 for comparison. It is seen that the mass fraction ϕ_2 increases linearly along the channel for $x/H > 5$, *i.e.* the fibers flocculate at nearly constant rate along the channel. Again, the random fiber orientation increases the formation of flocs right after the reinjection. The divergence of the mass fraction curves for the same cases but for the diffuser highlights the tremendous increase in the flocculation due to the decelerating flow in the diffuser.

Effects of fiber inertia and fiber orientation

We investigate the influence of fiber inertia on the formation of flocs for Case 2, where the reinjected fibers are randomly oriented, and Case 3, where the reinjected fibers are aligned with the longitudinal direction of the diffuser. The reference fiber inertia is altered by varying the fiber density ρ_f. We consider two additional instances, *i.e.* lower-inertia fibers ($\rho_f/5$) and higher-inertia fibers ($100\rho_f$).

Figure 7 shows the results for Case 2 for all three instances of fiber inertia. A high fiber inertia in combination with the random fiber orientation increases the floc formation in the inflow channel and the beginning of the diffuser region. An elevation in the flocculation rate is observed downstream $x/H > 5$ for all three instances of fiber inertia, and it is the highest for the case with reference inertia. This result

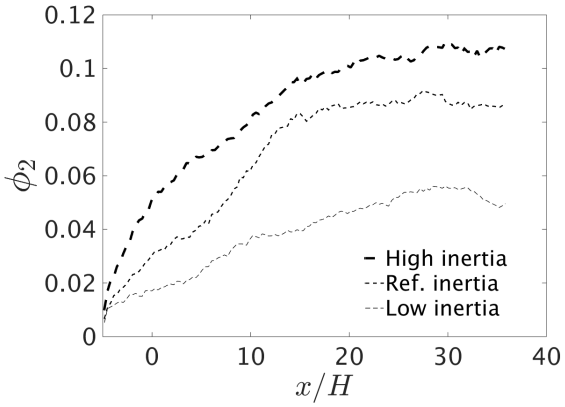

Figure 7. Mass fraction ϕ_2 along the length of the diffuser for different fiber inertia for Case 2.

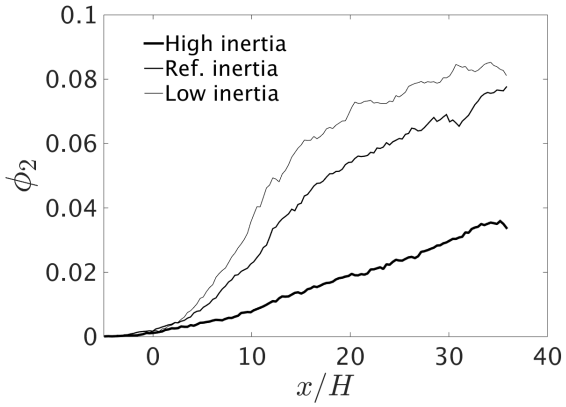

Figure 8. Mass fraction ϕ_2 along the length of the diffuser for different fiber inertia for Case 3.

implies that there is a critical fiber inertia that leads to greater flocculation in the diffuser.

Figure 8 illustrates the development of the mass fraction ϕ_2 for Case 3 for different fiber inertia. A low fiber inertia leads to greater flocculation in the diffuser downstream $x/H > 5$. We observe that for high-inertia fibers the floc mass fraction increases almost linearly in the whole computational domain. On the other hand, shorter response times of low-inertia fibers combined with decelerating flow field increases the probability of the fibers to form flocs.

Conclusions

This work investigates flocculation of rigid, straight fibers in the decelerating flow of an asymmetric planar diffuser. We use a particle-level rigid fiber model to carry out numerical analyses. Both the fiber inertia and the non-creeping fiber–flow interactions are taken into account. The fluid flow is described by the two-dimensional steady-state Navier–Stokes equation, and the standard k-ω turbulence model is used to account for the effects of turbulence. A stochastic model is employed to include the dispersion of fibers due to the turbulence. We consider dilute fiber suspensions and thus assume a one-way coupling between the fibers and the flow. The fibers interact through short-range attractive forces that cause them to form flocs whenever fiber–fiber contacts occur.

We demonstrate that the anisotropic hydrodynamic resistance of fibers and the flow velocity gradients govern the flocculation in the decelerating flow of an asymmetric diffuser. Hydrodynamically anisotropic fibers with finite inertia develop a relative velocity with respect to the carrying fluid while experiencing the flow gradients in the diffuser. This relative velocity generates the anisotropic hydrodynamic forces that cause ballistic deflection of fibers, which increases the inter-fiber collisions and thus increases the flocculation. Moreover, the kinematics of the reinjected fibers significantly affects the flocculation process in the inflow channel and at the entrance of the diffuser. A high fiber inertia and the random orientation of the reinjected fibers increase the formation of flocs in the region prior to the diffuser. Shorter fiber response times increase the flocculation for the fibers that are reinjected aligned with the longitudinal direction of the diffuser.

The results presented herein are of high relevance for the dry-forming process of pulp mats that involves air–fiber flowing suspensions.

References

[1] Andrić, J., Numerical modeling of air–fiber flows, PhD thesis, Chalmers University of Technology, Göteborg, Sweden, ISBN 978-91-7597-010-3, May 2014.

[2] Adin A., Asano T., The role of physical-chemical treatment in wastewater reclamation and reuse, *Water Science and Technology 37* (1998), pp. 79-90.

[3] Guibai L., Gregory J., Flocculation and sedimentation of high-turbidity waters, *Wat. Res. 25* (1991), pp. 1137-1143.

[4] Schmid C. F., *et al.*, Simulation of fiber flocculation: Effects of fiber properties and interfiber friction, *J. Rheol. 44* (2000), pp. 781-809.

[5] Switzer L.H., *et al.*, Handsheet formation and mechanical testing via fiber-level simulations, *Nord. Pulp Pap. Res. J. 19* (2004), pp. 434-439.

[6] Do-Quang M, *et al.*, Simulation of finite-size fibers in turbulent channel flows, *Phys. Rev. E 89* (2014), p. 013006.

[7] Jafari A., *et al.*, Multiscale modeling of fluid turbulence and flocculation in fiber suspensions, *J. Appl. Phys. 100*, (2006), p. 034901.

[8] Hämäläinen J., *et al.*, Papermaking fiber suspension flow simulations at multiple scales, *J. Eng. Math. 71* (2011) 1, pp. 55-79.

[9] Ramkrishna D., *Population balances–theory and applications to particulate systems in engineering*, Academic Press, San Diego, 2000.

[10] Andrić J., *et al.*, Ballistic deflection of fibres in decelerating flow, *Int. J. Multiphas. Flow 85* (2016), pp. 57-66.

[11] Wilcox D. C., *Turbulence modeling for CFD*, DCW Industries, Inc., California, 1993.

[12] Lindström S.B., Ueasaka T., Simulation of the motion of flexible fibers in viscous fluid flow, *Phys. Fluids 19* (2007), p. 113307.

[13] Andrić J., *et al.*, A study of a flexible fiber model and its behavior in DNS of turbulent channel flow, *Acta Mech. 224* (2013), pp. 2359-2374.

[14] Gosman A. D., Ioannides E., Aspects of computer simulations of liquid-fueled combustors, *J. Energy 7* (1983), pp. 482-490.

[15] Kim S., Karilla S.J., *Microhydrodynamics: Principles and Selected Applications*, Butterworth–Heinemann, Stoneham, 1991.

[16] Tritton D.J., *Physical fluid dynamics*, Clarendon, Oxford, 1988.

[17] Vega C., Lago S., A fast algorithm to evaluate the shortest distance between rods, *Computers Chem. 18* (1994), pp. 67-87.

[18] Buice C.U., Eaton J.K., Experimental investigation of flow through an asymmetric plane diffuser, *J. Fluids Eng. 123* (2001), pp. 819-828.

[19] Versteeg H.K., Malalasekera W., *An introduction to computational fluid dynamics*, Pearson Education Limited, 1995.

[20] Jasak H., Error analysis and estimation for the Finite Volume method with application to fluid flows, PhD thesis, Imperial College, University of London, 1996.

[21] Obi S., *et al.*, Experimental and computational study of turbulent separating flow in an asymmetric plane diffuser, in *9th Symposium on Turbulent Shear Flows*, Kyoto, Japan 16-19 August, 1993.

[22] El-Behery S.M., Hamed M.H., A comparative study of turbulence models performance for separating flow in a planar asymmetric diffuser, *Comput. Fluids 44* (2011), pp. 248-257.

Paper submitted: May 10, 2016
Paper revised: June 29, 2016
Paper accepted: June 29, 2016